Catalysis Science & Technology

Nitrogen and sulfur co-doping CeO2 nanorods for efficient photocatalytic VOCs degradation

Journal:	*Catalysis Science & Technology*
Manuscript ID	CY-ART-05-2022-000934.R1
Article Type:	Paper
Date Submitted by the Author:	26-Jun-2022
Complete List of Authors:	Yang, Hui; Yangzhou University, School of Chemistry and Chemical Engineering, Institute for Innovative materials and Energy Jia, Lu; Yangzhou University, School of Chemistry and Chemical Engineering Haraguchi, Jun; Kyushu Institute of Technology Wang, Yue; Yangzhou University, School of Chemistry and Chemical Engineering Xu, Bin; Yangzhou University, School of Chemistry and Chemical Engineering, Institute for Innovative materials and Energy Zhang, Qitao; Shenzhen University, Institute of Microscale Optoelectronics Nan, Zhaodong; Yangzhou University Zhang, Ming; Yangzhou University Ohno, Teruhisa; Kyushu Institute of Technology

ARTICLE

Nitrogen and sulfur co-doping CeO_2 nanorods for efficient photocatalytic VOCs degradation

Received 00th January 20xx,
Accepted 00th January 20xx

DOI: 10.1039/x0xx00000x

Hui Yang[a, c, 1], Lu Jia[a], Jun Haraguchi[c], Yue Wang[a], Bin Xu[a, *], Qitao Zhang[b, *], Zhaodong Nan[a], Ming Zhang[a], Teruhisa Ohno[c, *],

Ceria and its derivatives are environmentally-friendly and sustainable photocatalysts with strong oxygen storage/release ability, good photostability and high cost-effectiveness. In this work, nitrogen and sulfur synchronization doped ceria (NS-CeO_2) with a regular nanorod morphology was successfully prepared, in which doping was obtained just from one precursor and by one-step calcination treatment. The photooxidation performance of acetaldehyde on NS-CeO_2 was significantly better than that of undoped ceria. As confirmed by density functional theory (DFT) calculations, the oxygen atoms exposed on the surface are partially replaced after doping with nitrogen and sulfur, resulting in generating new impurity level states near the Fermi level and reducing the bandgap of NS-CeO_2. Meanwhile, the increased concentration of oxygen vacancies formed a doping transition state which can act as electrons captured center effectively. In addition, that transition state further exhibits media role of interfacial charge separation due to its effective restriction of recombination of electrons and holes, which can further improve the photocatalytic performance of NS-CeO_2. Herein, an effective strategy for synthesizing non-metallic doped CeO_2-based semiconductor photocatalysts that can degrade volatile organic compounds is proposed.

1. Introduction

The serious threat of global environmental pollution, especially pollution caused by volatile organic compounds (VOCs), has inspired researchers in various fields to develop more effective solutions for environmental pollution.[1-4] Photocatalysis technology has been well recognized as a promising solution and the use of photocatalysis technology is expected to increase.[5-8] Previous investigations of photocatalysts have mainly focused on traditional titanium dioxide (TiO_2), but its practical application has been seriously hindered by its wide band gap and low visible light absorption. Cerium oxide (CeO_2) belongs to a traditional n-type semiconductor with relatively flexible conversion ability between trivalent and tetravalent cerium oxidation states. While it also possesses some properties similar to those of TiO_2 such as chemical and physical stability, non-toxicity and low cost.[9, 10] That is to say CeO_2 has great potential as a promising photocatalyst for environmental management. Unfortunately, its photocatalytic efficiency is still inefficient due to its fast recombination rate of electron-hole pairs and low ratio of surface-active sites.[11, 12]

Hence, how to inhibit the recombination of carriers and how to enlarge the proportion of surface-active sites are research core points in the field of photocatalysis. Non-metallic doping has been proved to be one of the most effective methods for solving the issue of rapid electron/hole recombination. Doping can effectively reduce the band gap value of original CeO_2, thus later expanding the absorption spectrum from the ultraviolet light region to the visible light region, which is an important component of solar radiation. Non-metallic elements (such as B, C, N, F, P and S) with radii similar to the oxygen ions radius are introduced into the CeO_2 bulk by substituting oxygen from the lattice, which usually results in oxygen vacancies and structural defects.[13-15] These oxygen vacancies can result in the construction of a benefit transition state between the valence band and conduction band, which can act as electron capture centre and effectively slow down the recombination rate of photogenerated hole-electron pairs. In addition, it is also found that efficacious doping can significantly increase the concentration of trivalent cerium (Ce^{3+}) in CeO_2, which can further profitably delay the recombination efficiency of photoexcited electrons and holes.[16, 17]

For example, Zhang et al. used density functional theory calculation to reveal that doping nitrogen into CeO_2(110) induces new impurity level and reduces the activation energies, which facilitates water oxidation performance.[18] Mansingh et al. reported the preparation of N/S co-doped CeO_2 and their results showed that doped CeO_2 has improved photocatalytic activity for Cr (VI) reduction than pure CeO_2 under visible light irradiation, but the time durations of 24, 36 and 48 h for hydrothermal method was too lengthy.[19] Thus, doping of non-metallic elements is a common method for improving the photoelectric chemical properties of

[a] *School of Chemistry and Chemical Engineering, Institute for Innovative materials and Energy, Yangzhou University, Yangzhou 225002, China.*
[b] *International Collaborative Laboratory of 2D Materials for Optoelectronics Science and Technology of Ministry of Education, Institute of Microscale Optoelectronics, Shenzhen University, Shenzhen 518060, China.*
[c] *Department of Applied Chemistry, Faculty of Engineering, Kyushu Institute of Technology, Kitakyushu 804-8550, Japan.*
† Footnotes relating to the title and/or authors should appear here.
Electronic Supplementary Information (ESI) available: [details of any supplementary information available should be included here]. See DOI: 10.1039/x0xx00000x

semiconductor materials. How to introduce more catalyst active sites into catalytic reactions is also a tough nut to crack. Nanorod-like CeO_2 photocatalysts exhibit a high specific surface area and sufficient active sites, which may improve the photocatalytic performance by efficient light absorption.[20]

In this work, photocatalysts of regular CeO_2 nanorods doped with non-metallic nitrogen and sulfur under different calcination temperatures were successfully synthesized. Morphology and mapping images displayed that doped elements distributed evenly on the surface of NS-CeO_2 nanorods. DFT calculations verified that N and S co-doping can generate new impurity level states near the Fermi level, which effectually narrowing the band gap. Photooxidation performance of acetaldehyde (CH_3CHO) degradation was also confirmed. Active species trapping experiments also illustrated that superoxide radicals ($\cdot O_2^-$) and holes played a leading role in CH_3CHO degradation reactions. Therefore, doping with suitable nonmetallic elements is efficient for improving the photo-redox activity of other CeO_2-based semiconductor photocatalysts.

2. Experimental Section

2.1 Synthesis of photocatalysts

For a typical synthesis process, a glass bottle was filled with a mixture of 20 mL ethanol and 20 mL water, and 1,3,5-benzenetricarboxylic acid ($C_9H_6O_6$, 0.42 g, 2 mmol), cerium (III) nitrate hexahydrate ($Ce(NO_3)_3 \cdot 6H_2O$, 0.87 g, 2 mmol), 4-aminobenzenesulfonic acid ($C_6H_7NO_3S$, 0.52 g, 3 mmol) were dissolved in this mixture solution at the same time. Then the mixture was magnetically stirred at 70 ℃ for 3 hours. After the fully mixing reactions, the white precipitate was obtained by centrifugation and was washed with an ethanol: water (1:1, V/V) mixture for three times. Later, the precursor was dried overnight at 60 ℃ and then calcinated at different temperatures (600, 700 and 800 ℃) in an air atmosphere for 3 hours at a heating rate of 5℃·min^{-1}. Finally, N and S-co-doped CeO_2 (NS-CeO_2) products under different temperatures were obtained and kept for further use. For comparation, undoped CeO_2 products under different temperatures were also prepared without adding $C_6H_7NO_3S$ as precursor. In addition, before the activity test, the samples were irradiated under a UV lamp for 12 hours to remove organic adsorbates on the photocatalyst surface.

2.2 Characterization of photocatalysts

A powder X-ray diffraction (XRD) instrument (MiniFlex II, Rigaku Co., Japan) with CuKα (λ = 1.5418 Å) radiation (30 kV, 15 mA) was used for crystalline phase characterization. A UV-vis spectrometer (UV-2600, Shimadzu Co.) was used to measure the absorption properties. Morphology information and elemental mapping images were observed by SEM (Jeol, JSM-6701F) equipped with EDX component. X-ray photoelectron spectroscopy (XPS) was carried out on a Thermo scientific Escalab250Xi system at room temperature under 10^{-9} Pa using Al Kα radiation. Fourier transform infrared (FT-IR) spectra were measured from KBr pellets using a TENSOR27 system. Thermogravimetric (TG) analyses experiments were performed on PE Diamond TG/DTA with a heating rate of 10 ℃ /min under N2 atmosphere. photoluminescence (PL) spectroscopy measurement was performed at an excitation wavelength of 290 nm on a fluorescence spectrophotometer (Hitachi F-4500) at room temperature. Photocurrent measurements were performed on an electrochemical analyzer (HSV-110, Hokuto Denko Co.) in a standard three-electrode configuration with Pt as the counter electrode and Ag/AgCl as a reference electrode. Na_2SO_4 (0.1 M, PH = 6) aqueous solution was used as the electrolyte. The working electrode was irradiated by a Xe arc lamp (PXE-500, USHIO Inc.) and its intensity was controlled at 100 mW/cm^2. Meanwhile, a shutter was used to control the light switch every 20 s to test the photocurrent response.

2.3 Photooxidation experiment of CH_3CHO removal

Photocatalytic oxidation ability was assessed via decomposition of acetaldehyde (CH_3CHO, gas, Wako Chemical Reagent Co. Ltd). Firstly, 100 mg of prepared photocatalyst powder was spread on the bottom of a glass dish of 3 cm in diameter, and then the glass dish was placed in a Tedlar bag with a volume of 500 mL. Next, 500 ppm gaseous CH_3CHO with dry synthetic air filled was injected into the bag together, and the bag was then put into a dark box for 2 hours to reach an adsorption-desorption equilibrium. Then, an autonomous light-emitting diode lamp was used as a light source and its intensity was controlled at 0.6 mW/cm^2, which emitted light with a central wavelength of ca. 365 nm. At last, the real-time amount of generated CO_2 was measured by an on-line gas chromatograph (Agilent Technology 3000 A Micro-GC, FID detector).

2.4 Active species trapping experiments

Scavengers of tert-butanol (TBA), benzoquinone (BQ) and ethylene diamine tetraacetate acid disodium (EDTA) were applied for trapping hydroxyl radicals (·OH), superoxide radicals ($\cdot O_2^-$) and holes (h^+), respectively. All of the chemicals were bought from Wako Chemical Reagent Co. Ltd and they are analytical grade and could be used directly. In sequence, 100 mg of the photocatalyst and 1.0 mmol of each scavenger were dissolved in an ethanol/H_2O mixture (10 mL, v/v, 1:1) via stirring for 30 min and ultrasonic treatment for 20 min in order to obtain a uniform suspension. Then it was evenly coated and vacuum-dried at 90 ℃. Finally, the photooxidation CH_3CHO degradation for species trapping samples were also confirmed by the above test steps in ***2.3 section***.

2.5 Theoretical Calculation Details

We used the Vienna Ab initio Simulation Package (VASP) to perform all density functional theory (DFT) calculations within the generalized gradient approximation (GGA) using the Perdew-Burke-Ernzerhof (PBE) formulation. We chose the projected augmented wave (PAW) potentials to describe the ionic cores and take valence electrons into account using a plane wave basis set with a kinetic energy cutoff of 520 eV. The k mesh in Brillouin-Zone was set as $2\pi \times 0.03$Å^{-1}. Partial occupancies of the Kohn-Sham orbitals were allowed using the Gaussian smearing method and a width of 0.05 eV. The electronic energy was considered self-consistent when the energy change was smaller than 10^{-6} eV. A

geometry optimization was considered convergent when the force on each atom was smaller than 0.02 eV/Å.

3. Results and Discussion

3.1 Phase composition and morphology characterization

As shown in Fig. 1a, the XRD diffraction peaks of CeO_2 are approximately located at 28.54°, 33.18°, 47.49° and 56.37°, and they correspond to the crystal planes of (111), (200), (220) and (311), respectively.[21, 22] All diffraction lines are ascribed to the cubic fluorite structural CeO_2 phase (space group: Fm-3m (225)), which is well consistent with the standard data of JCPDS card (No. 00-034-0394). In addition, all of the diffraction peaks displayed no impurity peak of other phases, indicating that the sulfur and nitrogen co-doping has little effect on the crystal growth of CeO_2. However, in contrast to pure CeO_2, the highest peak (111) in the XRD pattern after doping shows a distinct shift to a lower angle under all calcination temperatures (Fig. 1b).[23] These apparent changes can be assigned to the successful introduction of sulfur and nitrogen into the crystal structure of CeO_2.

The optical impact of the incorporation of dopants into the CeO_2 lattice was also analysed by UV-vis absorbance spectra. Related results confirmed that the doping strategy can greatly enhance light absorption and induce narrowing of the bandgap value of CeO_2 (Fig. 1c). Moreover, the band gap value of NS-CeO_2 at 700℃ was calculated to be 2.98 eV, which is smaller than the bandgap values of other comparable samples (Fig. 1d). This result signifies that co-doping of nitrogen and sulfur in CeO_2 can induce smaller bandgap energy (E_g), which is recognized as one of the critical factors for enhancing the photooxidation efficiency ultimately.[24, 25]

As exhibited in Fig. 2a and Fig. S1, pure CeO_2 under different temperatures shows a nanorod morphology with a diameter of approximately 500 nm. After doping with nitrogen and sulfur, the products still maintain the nanorod-stacked structure.

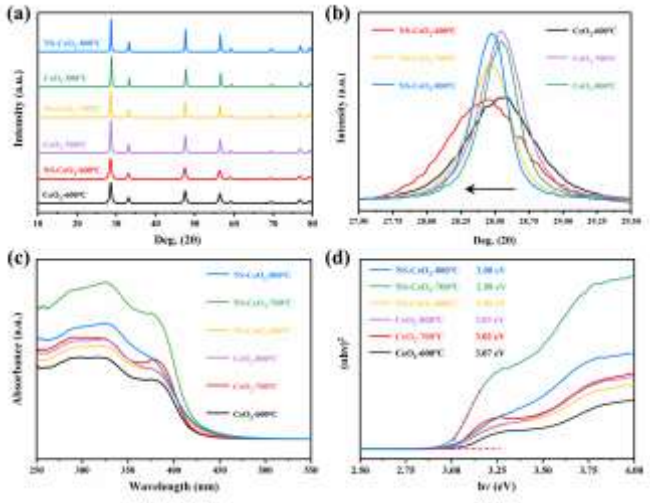

Fig. 1 (a) XRD patterns, (b) detailed view of the highest (111) peak patterns, (c) UV-vis absorption spectra and (d) Tauc plot analysis for band gap calculation of all samples.

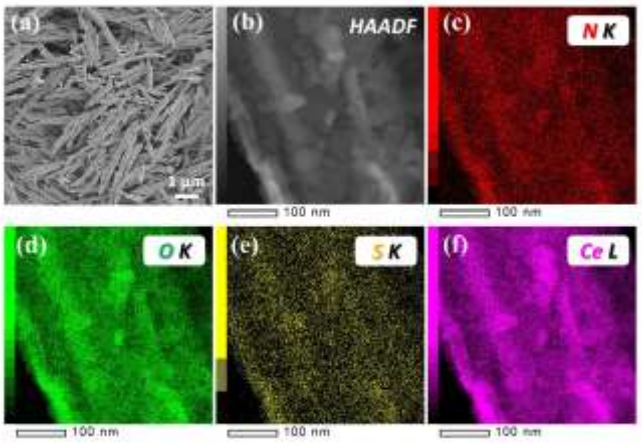

Fig. 2 (a) FE-SEM image, (b) HAADF image and (c-f) distribution of element mapping images of an NS-CeO_2 sample under the condition of a temperature of 700℃.

Furthermore, EDS mapping analysis (Fig.s 2b-f) indicated that after doping of nitrogen and sulfur, all the doping elements as well as Ce and O have a good distribution on the surface of NS-CeO_2 photocatalysts. And EDS spectra was used to confirm the superficial concentration of N and S dopant are about 6.34 and 1.66%, respectively (surface). XPS result displayed the value of N and S are about 5.32% and 1.78% in NS-CeO_2, respectively (surface). Organic element analysis (OEA) test measurement was applied to test the actual concentration of N (3.55%) and S (1.26%) dopant (bulk).

The surface chemical composition before and after nitrogen and sulfur doping were confirmed from XPS measurements (Fig. S3). As displayed in Fig. 3a, concentration of trivalent (denoted as (μ_0, ν_0), (μ_1, ν_1)) and tetravalent (denoted as (μ, ν), (μ_2, ν_2), and (μ3, ν3)) cerium was obtained after deconvolution treatment from XPS signals.[26, 27] The contents of Ce^{3+} and Ce^{4+} in pure CeO_2 were calculated to be 22.7% and 77.3%, respectively. While, the concentration of [Ce^{3+}] after N and S doping into CeO_2 reaches 31.8%, which is obviously increased than that in the undoped CeO_2 product. Meanwhile, these peaks display an evident shift to a lower binding energy (BE), manifesting that N and S are indeed doped into the lattice of CeO_2. Hence, it's understandable that the substitution of suitable dopants availably affects the chemical bond environment of Ce–O by the reduction from Ce^{4+} to Ce^{3+}, and this is also the primary cause of the concentration of oxygen vacancies ($O_{Vacancy}$) increased.[28, 29] In addition, three types of oxygen species from the O1s electron core level were confirmed after deconvolution, which can be ascribed to lattice oxygen ($O_{Lattice}$), oxygen vacancies ($O_{Vacancy}$) and active surface oxygen ($O_{Surface}$) (Fig. 3b).[28, 29] Compared with pure CeO_2, the BE of these oxygen species obviously shifts towards a higher BE after N and S doping. It should be noted that doping mainly affects the peak area (18.5%) of $O_{Vacancy}$, and the concentration in NS-CeO_2 is much superior than pure CeO_2 (7.78%). This may be because the introduction process can make up for the lack of doping-related charge and enhance the generation of $O_{Vacancy}$ in doped CeO_2. And the highly active $O_{Vacancy}$ can serve as active trapping centers for electrons and create a doping-induced transition state between the conduction band (CB) and valence band (VB).[23, 29] The transition state can efficiently inhibit the recombination of electron-hole pairs. Hence, it offers

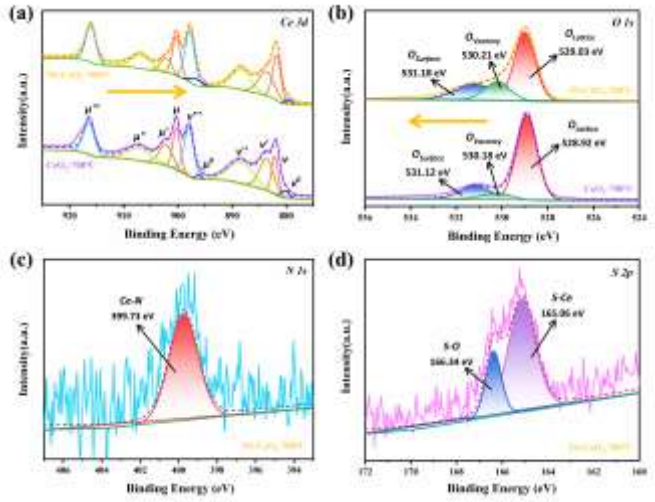

Fig. 3 High-resolution and separated peak curve XPS spectra of (a) Ce 3d, (b) O 1s, (c) N 1s and (d) S 2p.

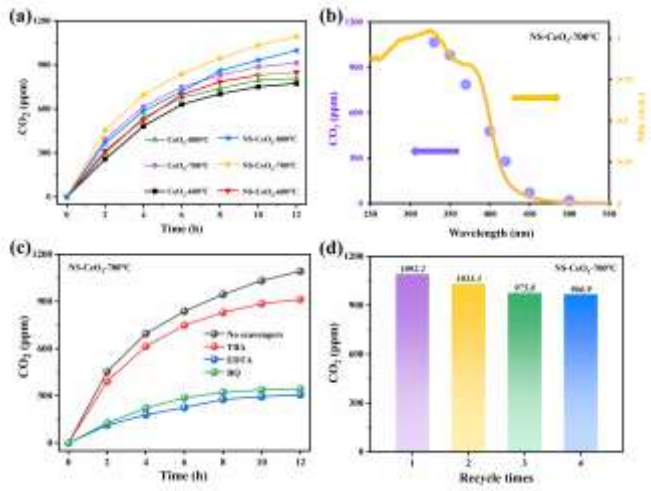

Fig. 5 (a) Time course of CO_2 generation curves of all samples, test of NS-CeO_2 sample under the condition of annealed temperature of 700 ℃ (b) Action spectra (c) CH_3CHO decomposition activities with the addition of EDTA, TBA and BQ sacrificial reagents and (d) Stability test.

strong evidence that doping of CeO_2 is in favour of improving photocatalytic activity when compared with pure CeO_2.

In addition, Fig. 3c displays the high-resolution peak of N 1s and the BE at 399.73 eV is well in conformity with the Ce-N bond into the CeO_2 crystallite.[30] Deconvoluted XPS spectrum of S 2p displayed two peaks at 166.34 and 165.06 eV, corresponding to S-O and S-Ce bonds,[19] which proves the presence of the S dopant at substitutional and interstitial sites of the NS-CeO_2 sample (Fig. 3d). Overall, N and S substitution of oxygen can form more trivalent cerium (Ce^{3+}) and facilitate the generation of oxygen vacancies ($O_{Vacancy}$). The potential of the conduction band (CB) was obtained from Mott-Schottky (M-S) plots test (Fig. S4) and ultraviolet photoelectron spectroscopy (UPS) of photocatalysts was further carried out to verify the specific location of band gap structure (Fig. S5). The results uncovered that the dopants are indeed introduced into the crystal lattice of CeO_2, leading to influence on the electronic properties of the nitrogen and sulfur co-doping products.

3.2 Investigation of photoelectric characteristics

As expressed in Fig. 4a, light-illuminated photocurrent response activity with time was performed to confirm the interface charge separation conditions. The photocurrent curves of products suddenly increase and decrease when the light is turned on and off, respectively, indicating their intrinsic properties of the semiconductor.[29, 31] The current intensity of NS-CeO_2 (275 μA/cm²) is higher than that of undoped CeO_2 (115 μA/cm²). More importantly, the intensity value of NS-CeO_2 is 2.67-times greater than that of commercial CeO_2 (102 μA/cm²). The superior intensity illustrates that these photoexcited electrons and holes in NS-CeO_2 are much more effectively separated and transferred than those in other comparable samples.

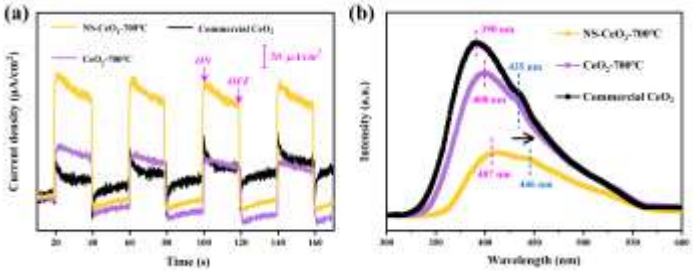

Fig. 4 (a) Transient photocurrent response and (b) steady-state photoluminescence spectra of NS-CeO_2, pure CeO_2 and commercial CeO_2.

Photoluminescence (PL) spectra were also frequently utilized to investigate the recombination efficiency of photogenerated electron-hole pairs.[29, 32] Commercial CeO_2 represents a stronger characteristic PL peak located at 390 nm and that is greatly attributed to intrinsic defects of CeO_2 (Fig. 4b). The weaker peak at 435 nm is mainly assigned to surface oxygen vacancies of CeO_2, which are existed between the O 2p valence band and the Ce 4f conduction band. [29] Also, pure and NS-doped CeO_2 samples all displayed with the same number of PL emission peaks. While the intensity was more distinctly decreased for NS-CeO_2 sample and suggested the lowest radiative recombination of the photoexcited carriers (e^- and h^+). It is notable that the characteristic peaks of CeO_2 and NS-CeO_2 red-shift from 400 nm to 407 nm, indicating their better visible light response ability. And the weaker peak shift from 435 nm (CeO_2) to 446 nm (NS-CeO_2), illustrating doping-related defect energy level in NS-CeO_2 is 0.07 eV below than CeO_2. In general, the above analysis indicated an excellent promotion of hole-electron pairs separation in NS-CeO_2 sample, which is beneficial for the photo-redox reactions and can efficaciously enhance the photocatalytic efficiency.

3.3 Photocatalytic CH_3CHO degradation activity

The photocatalytic removal efficiency was further assessed from degradation of gaseous acetaldehyde (CH_3CHO). Compared with pure CeO_2 annealed at various temperatures, the photocatalytic activity of NS-CeO_2 is obviously improved after N and S doping (Fig. 5a). The amount of CO_2 liberation reaches a maximum value (1092 ppm) for the NS-CeO_2 sample annealed at 700 ℃, which value also means CH_3CHO has been completely degraded within 12 h. The outstanding photocatalytic performance is attributed to the superior concentration of $O_{Vacancy}$, and the

results well meet with the results of XPS analysis. Action spectra were measured to analyse the quantum efficiency of NS-CeO_2 sample annealed at 700℃ irradiated by different wavelengths from 320 to 500 nm (Fig. 5b). Significantly, the CO_2 production gradually decreases when the irradiation light gradually transfers from the ultraviolet region to the visible region, and the trend is well consistent with the UV-vis curve. Thus, it can be further confirmed that the NS-CeO_2 photocatalyst exhibits a good light absorption dependence and it is indeed a valid photocatalytic process.

It is also essential to analysis the main active substances in the CH_3CHO degradation process by trapping experiments (Fig. 5c).[33-35] Before activity test, the surface water content of the photocatalyst was tested by TG and FTIR measurement (Fig. S6), which is one of the important source of hydroxyl radicals (·OH). When EDTA or BQ was added, the degradation efficiency decreased rapidly, indicating that h^+ and $\cdot O_2^-$ both display important effects in this photocatalytic oxidation reactions. However, CO_2 generation was mildly decreased after the addition of TBA, demonstrating ·OH is not the primary active substance in the CH_3CHO degradation processes. Hence, the results indicate that h^+ and $\cdot O_2^-$ are the main active species, while ·OH has minor effects during the process of degradation of CH_3CHO in the nitrogen and sulfur-co-doped CeO_2 system. Moreover, the amount of CO_2 liberation for NS-CeO_2 displays no distinct decrease after four cycles of CH_3CHO photooxidation degradation (Fig. 5d), indicating that this photocatalyst retains excellent photocatalytic recycle stability. The NS-CeO_2 photocatalyst as-discussed in this work performs much higher performance of CH_3CHO oxidation than that of commercial metal oxide photocatalysts such as TiO_2 (21 ppm), commercial CeO_2 (150 ppm), WO_3 (200 ppm) and Sm-doped CeO_2 (304 ppm).24, 29 And the specific reaction process is shown by the following equations (1-3):

$$CeO_2 + h\nu \rightarrow CeO_2\,[h^+(VB) + e^-(CB)] \quad (1)$$

$$O_2 + e^- \rightarrow \cdot O_2^- \quad (2)$$

$$CH_3CHO + \bullet O_2^-/\,h^+ \rightarrow 2\,CO_2 + 2\,H_2O \quad (3)$$

3.4 Theoretical calculations and possible photocatalytic mechanism

More importantly, the electronic influence of nitrogen and sulfur doping was further evaluated via the density functional theory (DFT) method.[18, 36] The magnitude of the charge transfer was further calculated by Bader charge quantitatively as follows: pure surface oxygen atom (1.19 e), single doped with N atom (1.04 e), single doped with S atom (1.05 e), co-doped with N atom (1.03 e), and co-doped with S atom (1.05 e) (Fig. 6a-b & Fig. S7). The results for charge density difference displayed in Fig. 6c-d illustrate that doping with either N or S can obtain electrons from substrate of CeO_2 and that the electrons transfer from internal CeO_2 (cyan area) to the N and S position (yellow region). In addition, pure CeO_2(111) is a semiconductor as can be seen from the results for total and partial density of states (DOS) results (Fig. S8). As represented in the DOS comparation results of all the samples, the position of Ce 4f conduction band changed more obviously. This is probably

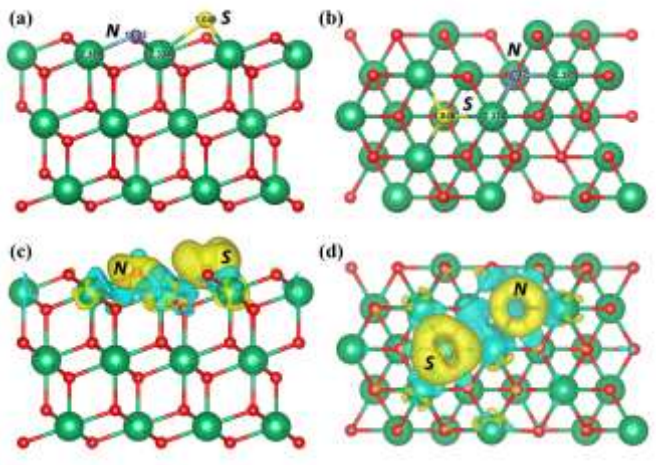

Fig. 6 (a, b) Bader charge diagram and (c, d) calculated charge density differences of NS-CeO_2 sample.

because the position of doping-related transition state exists closer to the conduction band of CeO_2 photocatalyst. After doping with N, new doping-related impurity level states near the Fermi level are gradually generated, but doping with S has little effect on the density of states of the system. This may be attributed to the smaller ionic radius of nitrogen (1.46 Å) than that of sulfur (1.84 Å), which is more suitable to replace oxygen (1.38 Å) incorporate into CeO_2 crystal lattice. Meanwhile, when N and S are doped at the same time, S has a certain degree of effect on doping-related impurity level and the band gap reduced tendency are consistent with the results of UV-vis spectra.

Based on results of the above-described characterization analysis and photocatalytic evaluation experiments, a proposed reaction mechanism of nitrogen and sulfur-co-doped CeO_2 is represented in Fig. 7. Substitution of N and S into the pure CeO_2 has an obvious influence on its cubic fluorite crystal structure. The oxygen atoms exposed on the surface are partially substituted by the N and S dopants, leading to an increased concentration of oxygen vacancies, which leads to the formation of doping-induced transition states. These increased oxygen vacancies can availably arrest electrons from the conduction band (CB) position and restrict the recombination of photo-excited electrons and holes for NS-

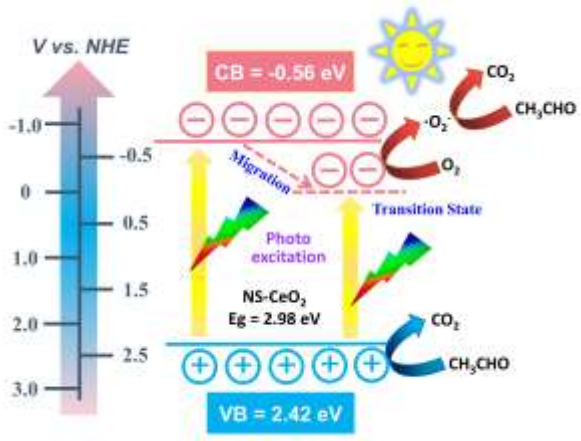

Fig. 7 A feasible mechanism for CH_3CHO degradation by NS-CeO_2 photocatalyst.

CeO_2 photocatalyst. This transition states induced by doping can prolong the lifetime of photo-excited carriers during the migration process and further effectively facilitate separation ability of those carriers. Furthermore, these separated electrons and holes involve in the photo-redox reactions to produce abundant reactive oxygen species (ROS), which are extremely vital to fully convert the toxic CH_3CHO VOCs to non-toxic CO_2 and H_2O. Based on the comparation results of CH_3CHO decomposition and degradation, we can conclude that the photooxidation efficiency is distinctly improved after nitrogen and sulfur synchronization doping. Hence, this effective non-metallic doping strategy is also feasible for traditional semiconductors to settle the matter of pollution caused by volatile organic compounds.

4. Conclusions

In conclusion, regular CeO_2 nanorod photocatalysts co-doped with non-metallic nitrogen and sulfur were successfully prepared. This convenient and advantageous preparation approach is cost-effective and can be easily popularized to fabricate other doped inorganic semiconductor materials. XPS results further indicated the surface chemical composition, the interactions and the concentration of oxygen vacancies before and after doping into CeO_2 photocatalysts. Morphology and mapping images displayed those doped elements are with a good distribution on the surfaces of NS-CeO_2 nanorods. DFT calculations verified that N and S co-doping can generate new doping-related impurity level states near the Fermi level, which will effectually reduce the band gap. It was also confirmed that NS-CeO_2 possesses superior photooxidation CH_3CHO decomposition performance compared with that of other CeO_2-based counterparts. Results of trapping experiments also indicated that superoxide radicals and holes played a vital role during degradation reaction progresses. In a nutshell, the non-metallic co-doped CeO_2 constructed in this work can provide an option to produce other kinds of synchronization doped photocatalysts for degrading VOC pollutions as well as other environmental protection and photo-electrocatalysis applications.

Author Contributions

Hui Yang, Bin Xu and Teruhisa Ohno designed this work. Jun Haraguchi, Lu Jia and Qitao Zhang characterized the photocatalysts. Hui Yang, Lu Jia, Yue Wang and Jun Haraguchi optimized reaction conditions and accomplished the reactions and substrate scopes. Hui Yang, Qitao Zhang, and Bin Xu co-wrote the manuscript. Teruhisa Ohno, Zhaodong Nan and Ming Zhang supervised the research. All of the authors discussed and commented on the manuscript.

Conflicts of interest

There are no conflicts to declare.

Acknowledgements

This work was financially supported by the Guangdong Basic and Applied Basic Research Foundation (2020A1515010982), Shenzhen Stable Support Project (20200812122947002), the National Natural Science Foundation of China (21805191), the Innovative Science and Technology Platform Project of Cooperation between Yangzhou City and Yangzhou University, China (No. YZ2020263), the Postgraduate Research &Practice Innovation Program of Jiangsu Province (Yangzhou University, KYCX21_3196), the Government Scholarship of Jiangsu Province (JS-2020-218), Yangzhou University International Academic Exchange Fund (YZUIAEF2021) and JST ACT-C program of Japan. The authors thank Dr. Nan Jian from the Electron microscope Centre of Shenzhen University.

Notes and references

1 A.H. Mamaghani, F. Haghighat, C.-S. Lee, Applied Catalysis B: Environmental, 203 (2017) 247-269.
2 L. Zhu, D. Shen, K.H. Luo, J Hazard Mater, 389 (2020) 122102.
3 X. Yue, N.L. Ma, C. Sonne, R. Guan, S.S. Lam, Q. Van Le, X. Chen, Y. Yang, H. Gu, J. Rinklebe, W. Peng, J Hazard Mater, 405 (2021) 124138.
4 S. Yuan, Q. Zhang, B. Xu, Z. Jin, Y. Zhang, Y. Yang, M. Zhang, T. Ohno, RSC Adv., 4 (2014) 62255-62261.
5 T. Montini, M. Melchionna, M. Monai, P. Fornasiero, Chem Rev, 116 (2016) 5987-6041.
6 J. Jacobsen, A. Ienco, R. D'Amato, F. Costantino, N. Stock, Dalton Trans, 49 (2020) 16551-16586.
7 S. Yuán, S. Liu, Q. Zhang, M. Zhang, B. Xu, T. Ohno, ChemCatChem, 10 (2018) 4269-4273.
8 R. Chen, J. Li, H. Wang, P. Chen, X.a. Dong, Y. Sun, Y. Zhou, F. Dong, Journal of Materials Chemistry A, 9 (2021) 20184-20210.
9 Z. Wang, R. Yu, Adv Mater, 31 (2019) e1800592.
10 Y. Zhang, S. Zhao, J. Feng, S. Song, W. Shi, D. Wang, H. Zhang, Chem, 7 (2021) 2022-2059.
11 R. Ma, S. Zhang, T. Wen, P. Gu, L. Li, G. Zhao, F. Niu, Q. Huang, Z. Tang, X. Wang, Catalysis Today, 335 (2019) 20-30.
12 D. Zhang, X. Du, L. Shi, R. Gao, Dalton Trans, 41 (2012) 14455-14475.
13 W.H.M. Abdelraheem, M.K. Patil, M.N. Nadagouda, D.D. Dionysiou, Applied Catalysis B: Environmental, 241 (2019) 598-611.
14 K. Kondo, N. Murakami, C. Ye, T. Tsubota, T. Ohno, Applied Catalysis B: Environmental, 142-143 (2013) 362-367.
15 A. Singhania, Industrial & Engineering Chemistry Research, 56 (2017) 13594-13601.
16 X. Xia, J. Li, C. Chen, Y.-P. Lan, X. Mao, F. Bai, Nanotechnology, 32 (2021).
17 P. Venkataswamy, D. Jampaiah, A.E. Kandjani, Y.M. Sabri, B.M. Reddy, M. Vithal, Research on Chemical Intermediates, 44 (2017) 2523-2543.
18 Y.-C. Zhang, Y.-K. Liu, L. Zhang, X.-t.-f. E, L. Pan, X. Zhang, A. Fazal e, D.-R. Zou, S.-H. Liu, J.-J. Zou, Applied Surface Science, 452 (2018) 423-428.
19 S. Mansingh, D.K. Padhi, K.M. Parida, Catalysis Science & Technology, 7 (2017) 2772-2781.
20 J. Hao, W. Zhan, L. Sun, G. Zhuang, X. Wang, X. Han, Inorg Chem, 59 (2020) 937-942.
21 J. Nie, G. Zhu, W. Zhang, J. Gao, P. Zhong, X. Xie, Y. Huang, M. Hojamberdiev, Chemical Engineering Journal, 424 (2021).
22 B. Xu, Q. Zhang, S. Yuan, S. Liu, M. Zhang, T. Ohno, Catalysis Today, 281 (2017) 135-143.
23 H. Yang, B. Xu, S. Yuan, Q. Zhang, M. Zhang, T. Ohno, Applied Catalysis B: Environmental, 243 (2019) 513-521.

24 B. Xu, H. Yang, Q. Zhang, S. Yuan, A. Xie, M. Zhang, T. Ohno, ChemCatChem, (2020) 2638-2646.
25 N. Tian, H. Huang, C. Liu, F. Dong, T. Zhang, X. Du, S. Yu, Y. Zhang, Journal of Materials Chemistry A, 3 (2015) 17120-17129.
26 B. Xu, Q. Zhang, S. Yuan, M. Zhang, T. Ohno, Applied Catalysis B: Environmental, 183 (2016) 361-370.
27 B. Xu, Q. Zhang, S. Yuan, M. Zhang, T. Ohno, Applied Catalysis B: Environmental, 164 (2015) 120-127.
28 A. Bahadoran, S. Ramakrishna, S. Masudy-Panah, J. Roshan De Lile, B. Sadeghi, J. Li, J. Gu, Q. Liu, Applied Surface Science, 568 (2021).
29 H. Yang, B. Xu, Q. Zhang, S. Yuan, Z. Zhang, Y. Liu, Z. Nan, M. Zhang, T. Ohno, Applied Catalysis B: Environmental, 286 (2021).
30 Z. Shen, Q. Xia, Y. Li, C. Yin, Z. Ge, X. Li, Y. Wang, Journal of CO_2 Utilization, 39 (2020).
31 H. Yang, L. Jia, Z. Zhang, B. Xu, Z. Liu, Q. Zhang, Y. Cao, Z. Nan, M. Zhang, T. Ohno, Journal of Catalysis, 405 (2022) 74-83.
32 Q. Zhang, S. Yuan, B. Xu, Y. Xu, K. Cao, Z. Jin, C. Qiu, M. Zhang, C. Su, T. Ohno, Catalysis Today, 315 (2018) 184-193.
33 S. Xiao, D. Pan, R. Liang, W. Dai, Q. Zhang, G. Zhang, C. Su, H. Li, W. Chen, Applied Catalysis B: Environmental, 236 (2018) 304-313.
34 S. Yuán, B. Xu, Q. Zhang, S. Liu, J. Xie, M. Zhang, T. Ohno, ChemCatChem, 10 (2018) 1267-1271.
35 Q. Zhang, B. Xu, S. Yuan, M. Zhang, T. Ohno, Catalysis Today, 284 (2017) 27-36.
36 Y. Xue, D. Tian, D. Zhang, C. Zeng, Y. Fu, K. Li, H. Wang, Y. Tian, Computational Materials Science, 158 (2019) 197-208.